Earth and Planetary Science Letters 392 (2014) 154–165

Contents lists available at ScienceDirect

Earth and Planetary Science Letters

www.elsevier.com/locate/epsl

A geochemical evaluation of potential magma ocean dynamics using a parameterized model for perovskite crystallization

Colin R.M. Jackson [a,*], Leah B. Ziegler [b], Hongluo Zhang [c], Matthew G. Jackson [d], Dave R. Stegman [e]

[a] Geological Sciences, Brown University, Providence, RI, USA
[b] CEOAS, Oregon State University, Corvallis, OR, USA
[c] Department of Earth Sciences, University of Minnesota, Minneapolis, MN, USA
[d] Department of Earth Sciences, UCSB, Santa Barbara, CA, USA
[e] Scripps Institution of Oceanography, UCSD, San Diego, CA, USA

ARTICLE INFO

Article history:
Received 14 August 2013
Received in revised form 26 December 2013
Accepted 17 January 2014
Available online 4 March 2014
Editor: L. Stixrude

Keywords:
early Earth
magma ocean crystallization
basal magma ocean
perovskite

ABSTRACT

Magnesium perovskite (MgPv) is likely the first phase to crystallize from a deep magma ocean. Consequently, MgPv crystallization has a strong control on the dynamics and chemical evolution associated with the earliest stages of silicate Earth differentiation. In order to better understand the chemical evolution associated with MgPv crystallization during a magma ocean, a parameterized model for major and trace element partitioning by MgPv has been developed. The parameterization is based on a compilation of published experimental data and is applied to batch and near-fractional crystallization scenarios of ultramafic liquids, allowing for a more complete analysis of the geochemical implications for magma ocean crystallization. The chemical signatures associated with modeled MgPv fractionation are evaluated in the context of possible dynamical outcomes to a magma ocean (e.g. basal magma ocean (BMO) or crystal settling). It is shown that fractionating MgPv from ultramafic liquids imparts diagnostic signatures (e.g. Ca/Al, HFSE anomalies, ε^{176}Hf–ε^{143}Nd) in both the liquid and solid phases. These signatures are not currently observed in the accessible Earth, suggesting that either early-fractionating MgPv was subsequently homogenized or crystal suspension was dominant during the earliest stages of magma ocean crystallization. A BMO that fractionates CaPv and MgPv is also considered and shown to mute many of unobserved geochemical effects associated with a MgPv-only fractionation, offering an alternative possibility for the evolution of a BMO depleted in heat producing elements.

1. Introduction

The accretion of Earth marked a period of rapid change, which ultimately set the initial conditions for subsequent geologic evolution. Our understanding of the earliest stages of Earth's history, however, remains largely incomplete and based on a limited set of observations. Accretionary scenarios posit Earth's formation proceeded with increasingly energetic collisions, and the last stages of accretion were likely energetic enough to melt large volumes of the mantle. These scenarios are supported by several independent lines of reasoning including the high pressure of core formation needed to explain abundance of moderately siderophile elements in the mantle (e.g. Li and Agee, 1996; Righter et al., 1997), evidence for a global magma ocean on the moon (e.g. Wood et al., 1970), and dynamical models of accretion (e.g. Chambers and Wetherill, 1998; Wetherill, 1985). Experimental and theoretical results suggest crystallization of liquids with compositions close to that of bulk silicate Earth (BSE) under lower mantle pressures begins with magnesium perovskite (MgPv) as the liquidus phase, which is followed at lower temperatures by ferropericlase (fP) and calcium perovskite (CaPv) (Andrault et al., 2011, 2012; de Koker et al., 2013; Fiquet et al., 2010; Ito et al., 2004; Liebske and Frost, 2012; Nomura et al., 2011; Presnall et al., 1998; Tronnes and Frost, 2002; Zhang and Herzberg, 1994). As such, MgPv likely dominated the chemical characteristics of the earliest forming solids following the putative terrestrial magma ocean. The chemical characteristics of this early-forming reservoir strongly influence the dynamics associated with, and immediately following, the crystallization of a deep magma ocean, which we consider here to be a complete or nearly complete melting of silicate Earth (e.g. Canup, 2004). Indeed, the distribution of major elements influences the density contrast between liquid and solid phases, and radioactive elements, such as U + Th, control the heat production within a particular phase. Moreover, fractionation of MgPv from a silicate liquid has consequences for the major and trace element composition and isotopic evolution that are implicit in

* Corresponding author. Tel.: +1 858 531 8544; fax: +1 401 863 2058.
E-mail address: colin_jackson@brown.edu (C.R.M. Jackson).

0012-821X/$ – see front matter
http://dx.doi.org/10.1016/j.epsl.2014.01.028

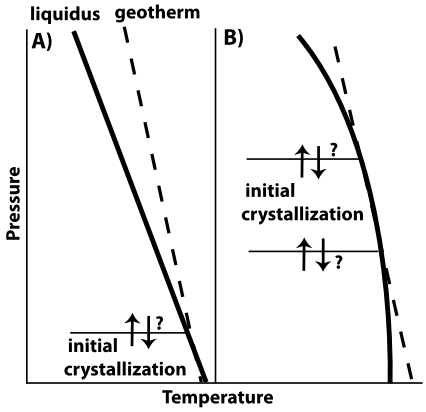

Fig. 1. Illustration of different dynamical possibilities for deep magma ocean crystallization. If the geotherm (dashed line) is always steeper than the mantle liquidus, crystallization will begin at the bottom of the mantle (A). The slope of the liquidus requires that there is a negative volume change upon crystallization, but the density of the solid phase can still be less than the liquid if heavy elements, like Fe, are abundant in the system and strongly partition into the liquid phase. If the mantle liquidus is highly curved relative to the geotherm, it is possible that the first crystallization will occur at mid-mantle depths (B). Again, depending on the relative densities of solid and liquid phases, it is possible for crystals to sink or float, although adiabatic sinking or floating will result in remelting of early forming crystals. It is also possible that the early-forming crystals remain entrained with the rapidly convecting magma ocean, and any crystal fractionation was a late stage process. Note that pressure increases downwards on the y-axis.

any dynamical outcome of magma ocean evolution. These elemental fractionations, once quantified, provide testable hypotheses associated with potential dynamical scenarios for magma ocean crystallization. The chemistry of MgPv crystallizing from a deep magma ocean, however, remains uncertain despite a growing body of experimental data collected under applicable pressures, temperatures (e.g. Agee, 1990; Andrault et al., 2012; Asahara et al., 2004; Corgne et al., 2005; Drake et al., 1993; Fiquet et al., 2010; Hirose et al., 2004; Ito et al., 2004; Ito and Takahashi, 1987; Kato et al., 1988a; Liebske et al., 2005; McFarlane et al., 1994; Nomura et al., 2011; Ohtani et al., 1998; Taura et al., 2001; Tronnes, 2000; Tronnes and Frost, 2002; Walter et al., 2004).

There are a series of plausible magma ocean crystallization scenarios (Fig. 1). At lower pressures, adiabatic temperature gradients ($\partial T/\partial P$) of silicate liquids are steeper than the liquidus of the mantle (Solomatov, 2000 and references within), resulting in a bottom-up crystallization sequence (Fig. 1A). At higher pressures, adiabatic and the mantle liquidus slopes are less certain (e.g. Andrault et al., 2011; Fiquet et al., 2010). It is possible that adiabatic temperature gradients remain steeper than the mantle liquidus to the bottom of the mantle (e.g. Andrault et al., 2011) and that minerals always remain dense compared to coexisting liquids (Thomas et al., 2012), potentially allowing large layers of MgPv to accumulate at the bottom of a deep magma ocean (Agee, 1990; Walter et al., 2004). Alternatively, it is also possible that the slope of the mantle liquidus becomes steeper than the adiabatic slope at pressures corresponding to the lower mantle (Fig. 1B; Mosenfelder et al., 2007, 2009; Stixrude et al., 2009), counter to the relative behavior expected for a shallow magma ocean. Under this circumstance, a deep magma ocean would begin to crystallize at a mid-mantle pressure and would proceed outward from this point, i.e. middle-out. The molar volume difference between silicate liquids and solids decreases with pressure due to the greater compressibility of liquids, and the density difference between liquids and MgPv can reverse if heavy elements, such as Fe, are strongly enriched in the liquid (Nomura et al., 2011; Stixrude et al., 2009). If the liquid–solid density contrast inverts at very high pressure (e.g. Sanloup et al., 2013), buoyant MgPv could then collect at a neutral buoyancy point under sub-liquidus temperatures, leading to a stable reef mid-mantle of MgPv during a magma ocean (Stixrude and Karki, 2005). This particular scenario has been termed a basal magma ocean (BMO) (Labrosse et al., 2007), and the later-forming, dense products of a BMO have been linked to lower mantle seismic structures (i.e. Garnero and McNamara, 2008), Earth's missing store of incompatible elements (i.e. Boyet and Carlson, 2005; O'Nions and Oxburgh, 1983), a primordial source for noble gases (Coltice et al., 2011), and a possible dynamo source region for Earth's ancient magnetic field (Ziegler and Stegman, 2013).

It is also possible that during deep magma oceans the density contrast between liquid and solid phases was sufficiently small and convective vigor was sufficiently high, that large volumes of MgPv remained entrained in the convecting silicate liquid. Segregation of crystals from melt would only occur once a critical threshold of grain size or crystallinity was reached (Solomatov and Stevenson, 1993; Tonks and Melosh, 1990). Under this scenario, the chemical evolution of the magma ocean would approach the batch (i.e. equilibrium) crystallization endmember until the point of crystal–liquid fractionation.

In all potential scenarios for deep magma ocean crystallization, the dynamics (e.g. crystal settling, floatation, or convective suspension, radiogenic heating) associated with the early crystallizing MgPv and equilibrium liquid are strongly controlled by their chemical compositions. Thus, evaluating the probability and ramifications of different deep magma ocean crystallization scenarios requires detailed predictions for the chemistry of MgPv, in addition to fP and CaPv, crystallizing from BSE liquid compositions under lower mantle conditions. In this study, we generate empirical parameterizations for major element and trace element partitioning by MgPv using experimental data collected under lower mantle conditions (multi-anvil and diamond-anvil apparatus). These parameterizations are then applied to a batch and near-fractional MgPv crystallization models in order to predict the distribution of major elements (Si, Al, Fe, Mg, and Ca) and trace elements (rare Earth elements (REEs) + Y, high-field strength elements (HFSEs), U + Th) between MgPv and liquid as a function of crystallinity. The combined effects of CaPv + MgPv crystallization on trace elements are also explored in the context of a BMO. The predicted trace element patterns associated with MgPv and MgPv + CaPv crystallization are applied to isotopic evolution models and compared to arrays of natural samples.

2. Methods

A database of experimentally generated MgPv–silicate liquid pairs was compiled (Agee, 1990; Andrault et al., 2012; Asahara et al., 2004; Corgne et al., 2005; Drake et al., 1993; Hirose et al., 2004; Ito et al., 2004; Ito and Takahashi, 1987; Kato et al., 1988a; Liebske et al., 2005; McFarlane et al., 1994; Nomura et al., 2011; Ohtani et al., 1998; Taura et al., 2001; Tronnes, 2000; Tronnes and Frost, 2002; Walter et al., 2004). The information compiled includes major element composition of MgPv, the major element composition of the equilibrium silicate liquid, and associated experimental parameters (i.e. temperature, pressure, capsule type, and run duration). When reported, trace elements partition coefficients were tabulated.

The compositions of the MgPv–silicate liquid pairs were used to define partition coefficients for major elements and trace elements. Major element partition coefficients were parameterized using both solid and liquid chemistry terms, and the trace elements were exclusively parameterized using $X_{\mathrm{sol}}^{\mathrm{Ca}}$ and $X_{\mathrm{sol}}^{\mathrm{Al}}$ terms. Parameterization coefficients for all elements are included in Table A.1. Only a subset of REE partition coefficients were parameterized, and the full REE suite was modeled as a coherent group by interpolating between the REEs with parameterizations. These

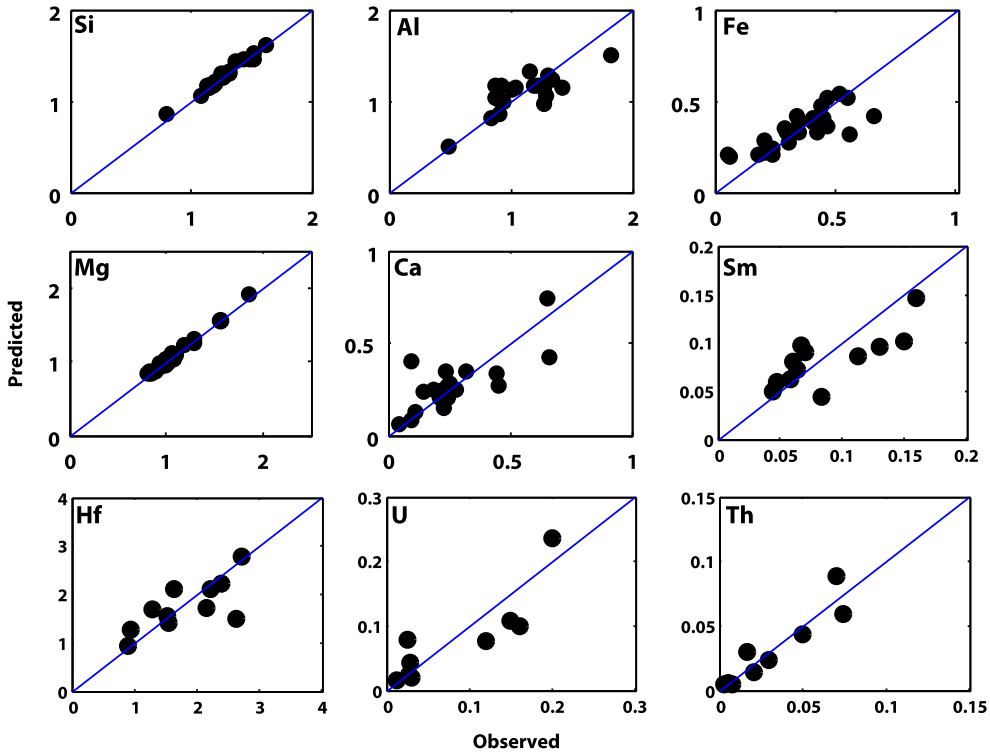

Fig. 2. Partition coefficient model fit comparison to database values. Plotted on the *x*-axis are the partition coefficients determined by experiment, and plotted on the *y*-axis are predictions for partition coefficients based on chemistry-based parameterizations. Major elements are plotted first and a selected set of trace elements (examples for actinides, REE, and HFSE) are plotted second.

REE partition coefficients, along with the remainder of trace element and major element partition coefficients, where applied to batch and near-fractional crystallization models to calculate the chemical evolution of a magma ocean crystallizing MgPv. Model uncertainties were assessed using a Monte-Carlo approach. Additional information regarding the modeling approach is provided in the Supplementary material.

3. Results

Fig. 2 compares observed (database values) and predicted (parameterized model) partition coefficients for the major elements and selected trace elements. Models for major components of MgPv (Mg and Si) show relatively good agreement between model prediction and observation, leading to small uncertainties in their predicted chemical evolution. The minor components (Al, Fe, and Ca) exhibit greater uncertainties associated with their parameterizations. Partitioning data collected at very high pressures and temperatures (up to 86 GPa and 3527 °C; Andrault et al., 2012; Nomura et al., 2011) using laser-heated diamond anvil cells (LH-DACs) are well explained by the chemistry-based model (Section 2), supporting the chemistry-based approach taken here.

The majority of coefficients for $X_{\mathrm{sol}}^{\mathrm{Ca}}$ and $X_{\mathrm{sol}}^{\mathrm{Al}}$ in the REE + Y parameterizations are positive, highlighting that REE + Y have similar substitutional mechanisms in both MgPv and pyroxene (e.g. Yao et al., 2012) and that Al plays a crucial role in charge balancing highly charged elements residing on the Mg site in MgPv (e.g. Liebske et al., 2005; Table A.1). HFSE (Nb, Ta, Zr, Hf, Ti) partition coefficients are also uniformly positive functions of $X_{\mathrm{sol}}^{\mathrm{Al}}$, but negative functions of $X_{\mathrm{sol}}^{\mathrm{Ca}}$, in line with the requirement for charge balancing when substituting for divalent elements (e.g. Mg^{2+}) and with the radius mismatch between Ca (larger) and HFSEs (smaller). For all HFSEs, the $X_{\mathrm{sol}}^{\mathrm{Ca}}$ coefficient is stronger than $X_{\mathrm{sol}}^{\mathrm{Al}}$. U + Th partition coefficients are positive functions of $X_{\mathrm{sol}}^{\mathrm{Al}}$ and $X_{\mathrm{sol}}^{\mathrm{Ca}}$, in line with the similar radius of Ca and U + Th and the requirement for charge balancing upon substitution.

The chemical evolution of silicate liquid and MgPv are modeled to 50% crystallinity. The results of the model are only applicable to a scenario where MgPv is the sole crystallizing phase. We estimate that fP saturates near 50% crystallinity by averaging the two highest pressure and temperature determinations of $K_{d\,\mathrm{fP\text{-}liq}}^{\mathrm{Mg}}$ and $K_{d\,\mathrm{fP\text{-}liq}}^{\mathrm{Fe}}$ (Nomura et al., 2011) and applying the following fP saturation criterion: $X_{\mathrm{liq}}^{\mathrm{Mg}} K_{d\,\mathrm{fP\text{-}liq}}^{\mathrm{Mg}} + X_{\mathrm{liq}}^{\mathrm{Fe}} K_{d\,\mathrm{fP\text{-}liq}}^{\mathrm{Fe}} = 1$. Pressure, temperature, and minor components, such as Al, in fP and are ignored in this calculation which likely leads to an overestimation of crystallization at fP saturation. This is a crude model for fP saturation, but it provides an estimate for the range of crystallinity where the MgPv-only crystallization model is directly applicable. If fP or CaPv saturation occurs earlier than 50% crystallinity, the modeled compositional evolution is only directly applicable up to that point.

Figs. 3 and 4 show the modeled major element evolution of the liquid and solid, respectively, between $F = 1$ (completely liquid) and $F = 0.5$. The initial liquids in these calculations are assumed to be either "peridotitic" (blue curves; McDonough and Sun, 1995) or CI chondritic after core subtraction (red curves, hereafter "chondritic;" Ito et al., 2004). The major difference between these two compositions is that the peridotitic composition has a higher Mg/Si ratio. The Ca/Al ratio of the peridotite composition is slightly greater, and the abundance of Ca and Al in the peridotitic composition are greater than that of the chondritic composition. We choose to model these two generic compositions because they represent a range of plausible bulk Earth compositions and allow a test of model sensitivity to changes in this initial condition.

All scenarios considered predict that Si is moderately compatible in MgPv, causing $X_{\mathrm{liq}}^{\mathrm{Si}}$ to decrease with crystallization. However, $K_{d\,\mathrm{MgPv\text{-}liq}}^{\mathrm{Si}}$ is ~0.2 greater in peridotite scenarios compared

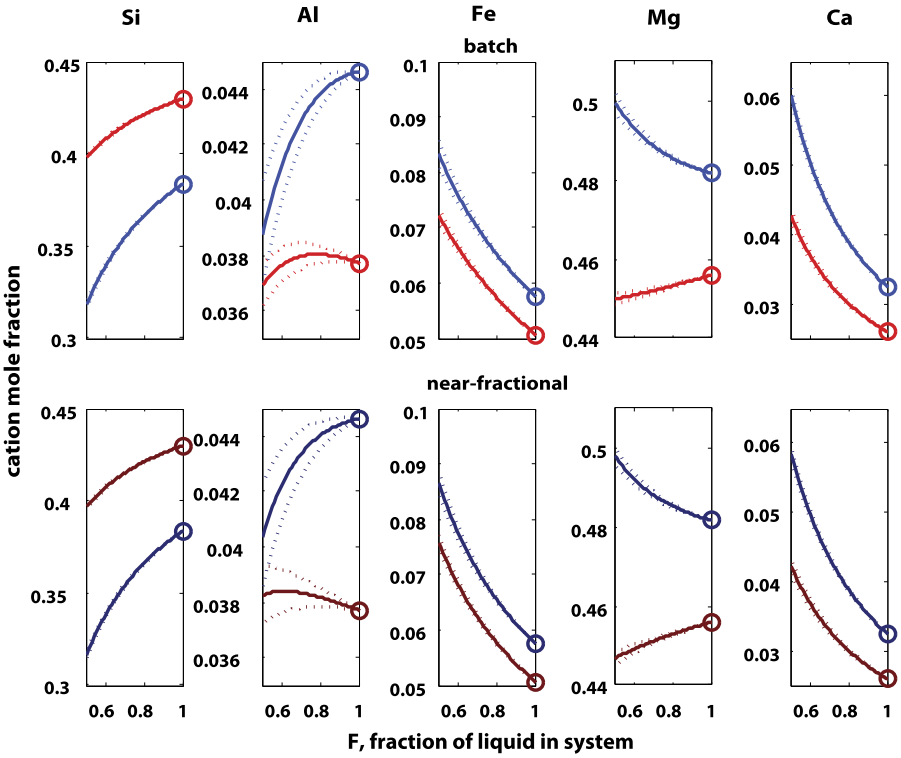

Fig. 3. Calculated average liquid composition evolution for different crystallization scenarios (solid lines). The top row shows liquid evolution under batch scenarios. The bottom row shows liquid evolution under near-fractional scenarios. Blue curves are for a peridotitic starting composition. Red curves are for a chondritic starting composition. The starting concentrations for each element are given by a color-coded symbol on the right y-axes. Dotted lines represent a one standard deviation envelope around the mean value as determined by the Monte Carlo approach. (For interpretation of the references to color in this figure legend, the reader is referred to the web version of this article.)

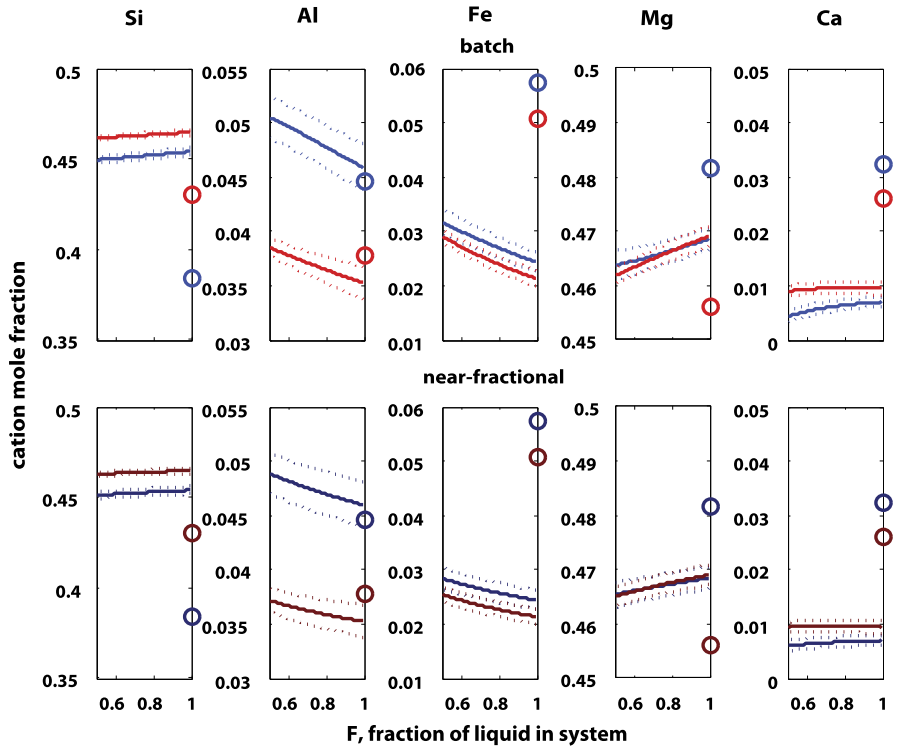

Fig. 4. Calculated average solid composition evolution for different crystallization scenarios (solid lines). The top row shows solid evolution under batch scenarios. The bottom row shows solid evolution under near-fractional scenarios. Blue curves are for a peridotitic starting composition. Red curves are for a chondritic starting composition. The starting concentrations for each element are given by a color-coded symbol on the right y-axes. Dotted lines represent a one standard deviation envelope around the mean value as determined by the Monte Carlo approach. (For interpretation of the references to color in this figure legend, the reader is referred to the web version of this article.)

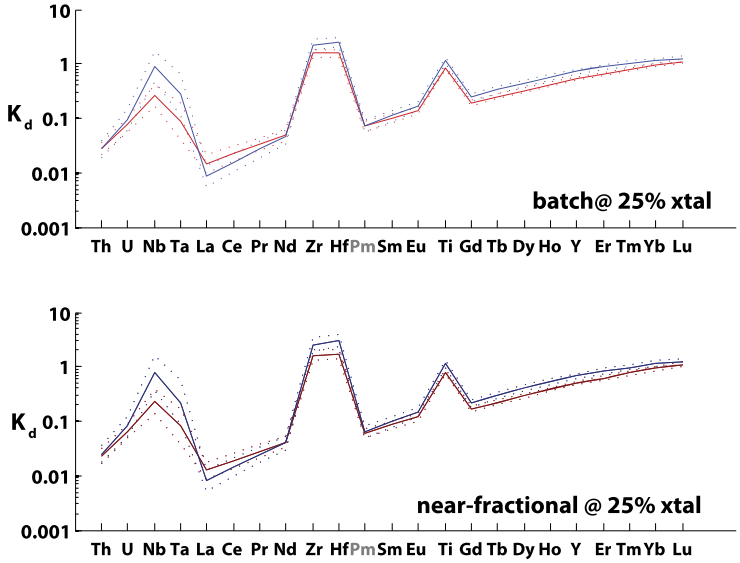

Fig. 5. Spidergram of modeled trace element partition coefficients for batch and near-fractional scenarios at 25% crystallinity. Blue curves are for a peridotitic starting composition. Red curves are for a chondritic starting composition. Peridotite and chondrite scenarios give similar REE + Y + U + Th partition coefficients, but HFSE partition coefficients are uniformly lower in the chondrite scenarios. Dotted lines represent a one standard deviation uncertainty estimate. (For interpretation of the references to color in this figure legend, the reader is referred to the web version of this article.)

to chondritic scenarios, which causes more rapid depletion of X^{Si}_{liq} compared to chondrite scenarios. Mg and Al partition nearly equally between MgPv and liquid, and can either be slightly incompatible or compatible depending on the specific chemistry of the system. Fe and Ca behave uniformly as incompatible elements in both peridotitic and chondritic scenarios (Fig. 3).

With increasing crystallization, the concentration of Fe increases in the both the liquid and solid, following a partition coefficient that decreases from ~0.4 to 0.3. The magnitude of decrease is greater in the near-fractional scenarios compared to batch. The earliest-forming MgPv possess a high Mg# compared to the equilibrium liquid (95 and 89, respectively), and this offset remains robust up to $F = 0.5$ (94 and 85, respectively). Thus, MgPv forming from $F = 1$ to 0.5 possesses a Mg# that is at least 5% greater than the present day convecting mantle.

Major element chemical variations stemming from different initial compositions and crystallization can affect how trace elements partition between MgPv and liquid. For example, HFSE partition coefficients are uniformly lower $(2 - 3x)$ in the chondrite scenarios (Fig. 5). This can be explained because lower X^{Ca}_{liq} and higher X^{Si}_{liq} in the chondrite scenarios combine to increase $K_{d\,MgPv\text{-}liq}^{Ca}$, and higher X^{Si}_{liq} causes $K_{d\,MgPv\text{-}liq}^{Al}$ to decrease. These shifts in partition coefficients, combined with a chondrite bulk composition, result in increased X^{Ca}_{sol}, but reduced X^{Al}_{sol}, for MgPv in chondrite scenarios. Given the compositional dependencies, this change in composition acts to lower HFSE partition coefficients. REE + Y + U + Th partitioning, however, is similar for both peridotite and chondritic bulk compositions because decreased X^{Al}_{sol} in the chondrite scenario is balanced by increased X^{Ca}_{sol}.

The model results indicate that there are several elemental and isotopic signatures that would be expected for a lithology enriched in MgPv. HFSEs are anomalously compatible in MgPv compared to elements with similar partition coefficients during MORB genesis, and a lithology enriched in MgPv should correspondingly contain relatively high concentrations of these elements (see Fig. 5 for a spidergram of partition coefficients at 25% crystallinity). Nb appears to be more compatible than Ta. This partitioning behavior would result in high Nb/Ta for MgPv and low Nb/Ta for the equilibrium liquid. Fractionations of Hf and Zr are less extreme but favor low Zr/Hf in MgPv. REE partition coefficients follow a pattern similar to pyroxenes, where the light REE are more incompatible compared to heavy REE. This pattern for REE partitioning, with high Sm/Nd in MgPv, would lead to a high (geochemically depleted) time-integrated $^{143}Nd/^{144}Nd$ isotopic signature for MgPv fractionating from a liquid with chondritic REEs. Conversely, the relative partitioning of Lu and Hf leads to low Lu/Hf in MgPv. Given time, this indicates that MgPv would evolve low (enriched) time-integrated $^{176}Hf/^{177}Hf$ signatures.

The database of perovskite–silicate liquid experimental data and crystallization model codes are freely available upon request.

4. Discussion

The following section provides an analysis of possible geochemical consequences associated with a bottom-up magma ocean and BMO crystallization (middle-out) scenario. It is shown that a BMO should enrich the accessible Earth (mantle sampled by volcanism + xenoliths and crust) in MgPv and that this enrichment would impart major element, trace element, and isotopic signatures that are not observed. MgPv sequestration associated with a bottom-up crystallization scenario is also shown to impart diagnostic geochemical signatures for the accessible Earth that are not observed, consistent with previous analysis of this dynamical possibility (e.g. Corgne et al., 2005; Kato et al., 1988b; Walter et al., 2004; Drake et al., 1993; Liebske et al., 2005).

These conclusions are critically dependent on over-arching assumptions:

(1) The following geochemical arguments are essentially based on mass balance, and thus, require an estimate for the composition of BSE. Geochemical arguments presented here are generally based on lithophile (not partitioned into the core), refractory (little modified by volatility-controlled fractionations during accretion) elements. Consequently, uncertainties associated with mass balance arguments using these elements are minimized compared to arguments based on more volatile and/or siderophile elements.
(2) Elemental fractionations and associated isotopic evolution are predicted using partition coefficients ultimately derived from

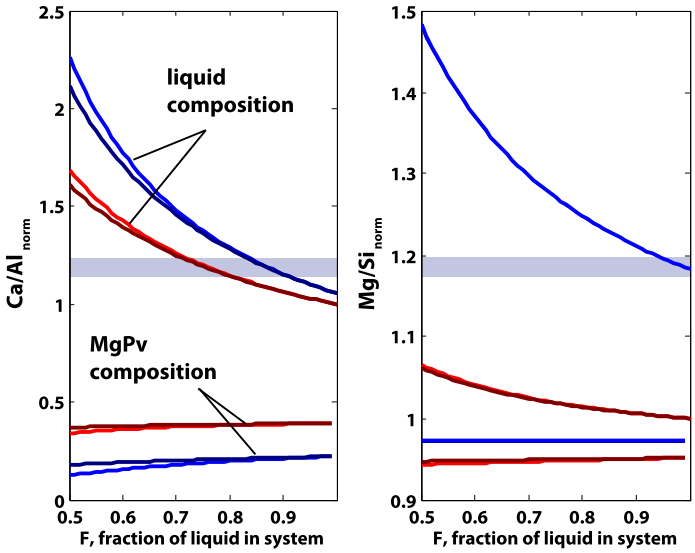

Fig. 6. Liquid and solid evolution with MgPv crystallization for Ca/Al (left) and Mg/Si (right). Calculations are normalized to CI composition given by Ito et al. (2004). Blue curves are for a peridotitic starting composition. Red curves are for a chondritic starting composition. Lighter shades are for batch calculations, and darker shades are for near-fractional calculations. The transparent blue bands represent the accessible Earth composition (taken from Walter et al., 2004, Table 9, CM1). Compared to both BSE compositions explored in this study, the accessible Earth has high Ca/Al. Subtraction of MgPv from the accessible Earth can help reconcile this difference. Adding MgPv to the accessible Earth via a BMO will correspondingly lower Ca/Al, causing sub-chondritic Ca/Al for the accessible Earth. Uncertainties have been omitted for clarity. (For interpretation of the references to color in this figure legend, the reader is referred to the web version of this article.)

the parameterization of existing experimental data presented in Section 3. The majority of the data were collected at pressures and temperatures associated with the uppermost lower mantle. Although the current model can explain data collected at higher pressure and temperatures (Andrault et al., 2012; Nomura et al., 2011), model predictions for a bottom-up magma ocean and late-stage BMO require substantial extrapolation in pressure and temperature.

4.1. Chemical signatures associated with the early stages of a magma ocean

A magma ocean and concurrent core formation represent periods when massive amounts of material was redistributed within Earth and are correspondingly plausible mechanisms for forming and sequestering large geochemical reservoirs. It is remains possible that the dynamics of a deep magma ocean resulted in the concentration of either MgPv or a dense silicate liquid at or near the bottom of the mantle. If silicate liquid concentrated at the bottom of the magma ocean during MgPv crystallization, this reservoir will be depleted in MgPv and correspondingly enriched in CaPv and fP components. By mass balance, the mantle overlying the dense silicate liquid becomes enriched in MgPv. This generic scenario is analogous to a BMO. If MgPv becomes concentrated at the bottom of a magma ocean, this necessarily depletes the overlying mantle in MgPv and enriches it in CaPv and fP components. If a reservoir of concentrated silicate liquid or MgPv remains sequestered to the present day, its existence will be reflected in the composition of accessible Earth by the absence of the sequestered chemical components. MgPv fractionates certain trace and major elements efficiently. Thus, the addition or subtraction of MgPv from the accessible Earth leads to diagnostic geochemical signatures that are associated with different potential scenarios for magma ocean evolution. The following sections explore the predicted geochemical consequences associated with the addition and subtraction of MgPv from the accessible Earth.

4.1.1. Major element signatures associated with MgPv subtraction from the accessible Earth

Crystal fractionation of dense MgPv from a magma ocean necessarily involves subtracting MgPv from the accessible Earth. This process can be modeled by assuming the present-day accessible Earth represents the bulk liquid in equilibrium with the crystallizing MgPv and that this MgPv now constitutes a hidden reservoir.

Both Ca and Al are refractory, lithophile elements, and accretion and core formation should not have fractionated these elements. Therefore, the Ca/Al of the Earth is expected to be equal to Ca/Al of chondrites (e.g. McDonough and Sun, 1995). This, however, is not uniformly supported by observations, at least for the accessible Earth; i.e. there is evidence that $Ca/Al_{accessible\ Earth}$ is greater than $Ca/Al_{chondrite}$ (e.g. Walter et al., 2004). From Fig. 6, it can be seen that the subtraction of ~10–20% MgPv from a magma ocean results in Ca/Al for the liquid equal to $Ca/Al_{accessible\ Earth}$ (e.g. Walter et al., 2004). This is consistent with the hypothesis that the terrestrial magma ocean led to the sequestration of a MgPv-rich reservoir. $Mg/Si_{accessible\ Earth}$ is too high to be inherited directly from chondrites, but volatility controlled fractionation and core formation—processes that increase Mg/Si_{BSE}—may explain super-chondritic $Mg/Si_{accessible\ Earth}$ (e.g. Lodders, 2003; Rubie et al., 2011). Nonetheless, 10–20% fractionation of MgPv from a chondritic liquid has only a small effect on $Mg/Si_{accessible\ Earth}$ (Fig. 6).

4.1.2. Major element signatures associated with MgPv addition to the accessible Earth

A BMO is a hypothesized outcome to a magma ocean where crystallization initiates in the mid-mantle and MgPv is buoyant (e.g. Labrosse et al., 2007). This leads to an overlying layer that is enriched in MgPv and an underlying liquid layer depleted in MgPv (correspondingly enriched in fP and CaPv components). This overlying MgPv layer homogenizes with the remaining mantle, effectively adding MgPv to the accessible Earth. Due to Fe incompatibility during crystallization, the density contrast between later-forming liquid and MgPv may have become sufficiently large that the dense liquid layer became convectively isolated from the overlying mantle. Our major element modeling shows that MgPv is a low Mg/Si and Ca/Al phase compared to the BSE. Thus, the enrich-

ment of MgPv in the accessible Earth, via a BMO, acts to lower $Mg/Si_{accessible\ Earth}$ and $Ca/Al_{accessible\ Earth}$ (Fig. 6). These shifts relative to proposed bulk Earth compositions are not observed. Thus, a BMO where only MgPv is fluxed into the accessible Earth causes fractionations of refractory, lithophile major elements, which are not observed.

4.1.3. Trace element and isotopic signatures associated with MgPv fractionation

The HFSEs are preferentially incorporated into MgPv compared to elements of similar incompatibility during the generation of MORB. This type of partitioning behavior results in strong positive concentration anomalies for HFSEs in MgPv and correspondingly strong negative anomalies in liquids solely saturated in MgPv. Thus, the addition of MgPv to the accessible Earth results in positive HFSE anomalies, whereas the subtraction of MgPv from the accessible Earth results in negative HFSE anomalies. Studies defining the trace element abundances of the accessible Earth (e.g. McDonough and Sun, 1995) indicate that HFSEs are not uniformly concentrated or depleted in the accessible Earth, providing a robust argument against any large scale enrichment or depletion of MgPv.

The combined $\varepsilon^{176}Hf$–$\varepsilon^{143}Nd$ isotopic system provides a time-integrated record of HFSE–REE fractionation not obscured by partial melting. As such, $\varepsilon^{176}Hf$–$\varepsilon^{143}Nd$ systematics of mantle rocks can also be used as a robust indicator of MgPv fractionation (e.g. Salters and White, 1998). This is explored further below in the context enriching or depleting the accessible Earth in MgPv.

4.1.3.1. Hf–Nd isotopic signatures associated with MgPv addition to the accessible Earth The accessible Earth shows small positive $\varepsilon^{142}Nd$ ($\sim 0.18 \pm 0.05$ ε units) anomalies compared to ordinary chondrites (Boyet and Carlson, 2005). Assuming that the excess ^{142}Nd in the accessible Earth is the result of ^{146}Sm decay, and not the result of poor mixing of a nucleosynthetically-heterogeneous solar nebula (Huang et al., 2013; Ranen and Jacobsen, 2006), this suggests that either the Earth contains a hidden enriched reservoir with corresponding negative $\varepsilon^{142}Nd$ anomalies (Boyet and Carlson, 2005), that the Earth lost an enriched reservoir to space due to collisional erosion (O'Neill and Palme, 2008), or that the Earth accreted with Sm/Nd slightly higher (~5–7%) than chondrites (e.g. Caro and Bourdon, 2010). Importantly, despite the evidence for a net-depleted accessible Earth, arrays of $\varepsilon^{176}Hf$–$\varepsilon^{143}Nd$ from mantle-derived materials cross near the origin (Blichert-Toft and Albarede, 1997; Vervoort and Blichert-Toft, 1999; Bouvier et al., 2008; Chauvel et al., 2008). This is evidence that the mechanism responsible for the elevated terrestrial $\varepsilon^{142}Nd$ did not substantially decouple $\varepsilon^{176}Hf$ and $\varepsilon^{143}Nd$ systems (e.g. Caro and Bourdon, 2010). Indeed, the majority of variance from a CHUR model that is observed in modern-day, mantle-derived rocks can be explained by coupled fractionations of Lu/Hf and Sm/Nd ultimately associated with partial melting of the upper mantle.

The BMO scenario has been proposed as a physical process that is capable of generating a hidden enriched reservoir (negative $\varepsilon^{142}Nd$ anomalies) during the earliest stages of Earth's history (Labrosse et al., 2007). Applying the modeled trace element partition coefficients from Section 3, it is clear that enrichment in MgPv can impart geochemically-depleted (positive) $\varepsilon^{142}Nd$ and $\varepsilon^{143}Nd$ signatures for the accessible Earth, in agreement with the analysis of Labrosse et al. (2007; Fig. 7). Given the partitioning of Lu and Hf by MgPv, however, it is also predicted that an enrichment in MgPv results in geochemically-enriched (negative) $\varepsilon^{176}Hf$ for the accessible Earth. Thus, MgPv fractionation effectively decouples Nd and Hf isotopic systems, and this is a distinctive signature of MgPv (Blichert-Toft and Albarede, 1997; Salters and White, 1998; Walter et al., 2004).

The magnitude of the decoupling between $\varepsilon^{176}Hf$ and $\varepsilon^{143}Nd$ by MgPv fractionation can be quantified using the initial conditions proposed for a BMO. The starting volume of the BMO is estimated to be approximately 25% of the mantle or 1.21×10^{24} kg (liquid density = 5000 $kg\,m^{-3}$) in order to impart a super-chondritic (~5–7%) Sm/Nd ratio for the accessible Earth (Labrosse et al., 2007). LLSVPs and ULVZs constitute <3 vol% of the mantle (Burke et al., 2008), implying at least 1.06×10^{24} kg of MgPv (22 vol% of mantle, density = 5000 $kg\,m^{-3}$; Stixrude et al., 2009) was added into the accessible silicate Earth (3.20×10^{24} kg) under the MgPv-only crystallization BMO hypothesis (Labrosse et al., 2007).

The composition of the MgPv added to the accessible Earth via a BMO has been calculated using batch and near-fractional crystallization approaches. The partition coefficients for the batch calculation are taken from the batch MgPv crystallization model (Section 3) at $F = 0.5$. The partition coefficients for the near-fractional calculation are taken from the near-fractional MgPv crystallization model (Section 3), but vary with F up to $F = 0.5$. After $F = 0.5$, the partition coefficients are taken as constant, using the values from $F = 0.5$. These partition coefficients were then applied to calculate the trace element patterns of the MgPv and liquid after 90% crystallization (22 vol% crystallized out of 25 vol% initially). These compositions of MgPv are then mixed with a reservoir of primitive mantle (representing the mantle overlying the BMO) to calculate the composition of the accessible Earth that results from a MgPv-only BMO. We then calculate the resulting isotopic evolution for the accessible Earth from 4 Ga to present day and compare the results to CHUR evolution models. The time frame of 4 Ga to present-day was chosen to account for the fact that a BMO should solidify over a relatively long time compared to a bottom-up magma ocean.

Fig. 7 shows the effects of adding MgPv to the accessible Earth via a BMO. Because the added MgPv has low $\frac{Lu/Hf}{Sm/Nd}$ relative to chondritic values, it displaces bulk $\varepsilon^{176}Hf$–$\varepsilon^{143}Nd$ for the accessible Earth from the origin, toward the lower-right quadrant. The hidden BMO products are displaced into the upper-left quadrant (not plotted) by mass balance. Subsequent differentiation of the accessible Earth, including crustal extraction (and associated partial melting of peridotite) and crustal recycling would generate an $\varepsilon^{176}Hf$–$\varepsilon^{143}Nd$ array of OIB and MORB compositions that is anchored by the modeled accessible Earth value (Fig. 7). Scenarios that produce bulk accessible Earth values for $\varepsilon^{176}Hf$–$\varepsilon^{143}Nd$ that are significantly displaced from the present day accessible Earth array can be rejected.

For a BMO that fractionates to $F = 0.1$, the vector for MgPv addition to the accessible Earth is nearly horizontal but still toward the lower-right quadrant. The vector for a BMO that fractionated to a higher F (less crystallization) has a more negative slope compared to that calculated for $F = 0.1$. To keep $\varepsilon^{176}Hf$–$\varepsilon^{143}Nd$ coupled, the MgPv addition vector would have to be toward the upper-left apex, which is not predicted. Explaining the apparent ~5–7% increase of Sm/Nd for the accessible Earth, which results in an $\varepsilon^{143}Nd = +5$ to $+9$, via a MgPv-only BMO would displace the array of $\varepsilon^{176}Hf$–$\varepsilon^{143}Nd$ mantle values significantly off of the observed mantle array.

We stress that this analysis does not require that a BMO never occurred. Rather it argues that a MgPv-only BMO is not likely to generate a hidden geochemical reservoir that balances the apparent depletion of $\varepsilon^{142}Nd$ in the accessible Earth. It is possible that a BMO did occur, but the geochemical consequences are muted because nearly all materials processed through the BMO have now been homogenized with the remaining mantle. It is also possible that the BMO volume was significantly less than the proposed 20–25%, making the associated fractionations smaller, and more difficult to observe, than modeled here.

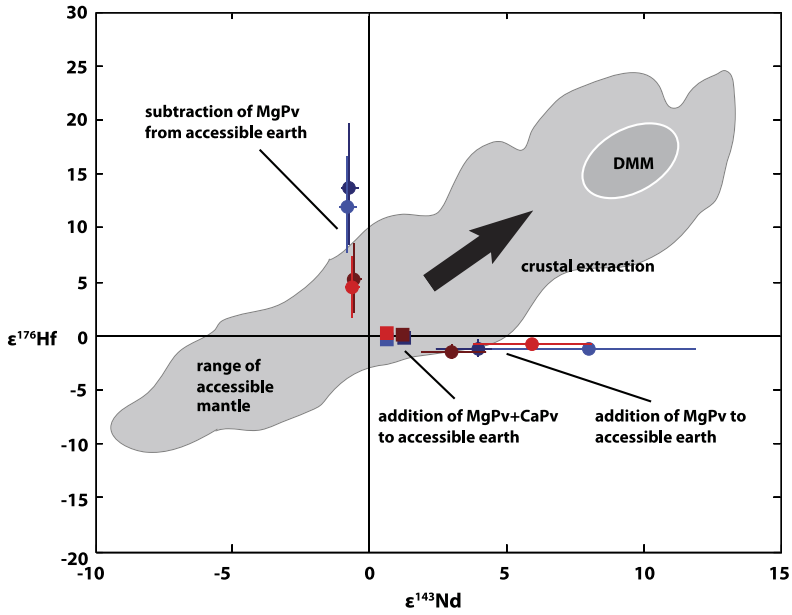

Fig. 7. ε^{176}Hf–ε^{143}Nd plot of observed mantle compositions (grey field, redrawn from Bouvier et al., 2008), overlain by model results for different MgPv fractionation scenarios. Blue dots are for a peridotitic starting composition. Red dots are for a chondritic starting composition. Lighter shades are for batch calculations, and darker shades are for near-fractional calculations. Dots in the upper-left quadrant are the time-integrated ε^{176}Hf–ε^{143}Nd effects of 10% MgPv subtraction from the accessible Earth. Dots in the lower-right quadrant are the time-integrated ε^{176}Hf–ε^{143}Nd effects for MgPv addition to the accessible Earth (BMO hypothesis). Compositions are calculated for a 25 vol% BMO that fluxes the first 90% of crystals formed into the accessible Earth. In all cases ε^{176}Hf and ε^{143}Nd are decoupled, shifting the modeled bulk accessible Earth composition off of the present day mantle array. Squares are modeled bulk accessible Earth compositions for an $F = 0.1$ BMO that fluxes 92.5% MgPv and 7.5% CaPv into the accessible Earth. Isotopic evolution for the accessible Earth in the BMO scenarios follow CHUR from until 4 Ga, and then deviate from CHUR following calculated Lu/Hf and Sm/Nd ratios. CHUR evolution parameters are taken from Bouvier et al. (2008). Uncertainties on individual scenarios are those propagated from uncertainties in partition coefficients (one standard deviation). (For interpretation of the references to color in this figure legend, the reader is referred to the web version of this article.)

4.1.3.2. Hf–Nd isotopic signatures associated with MgPv subtraction from the accessible Earth Subtraction of MgPv from the accessible Earth also has large consequences for ε^{176}Hf–ε^{143}Nd (e.g. Salters and White, 1998; Walter et al., 2004). Fig. 7 shows the predicted ε^{176}Hf–ε^{143}Nd composition of the accessible Earth after 10% subtraction of MgPv at 4.5 Ga. Even as little as 5% subtraction displaces the accessible Earth ~6 ε^{176}Hf units above the origin in peridotite scenarios. There is some suggestion that ε^{176}Hf $-\varepsilon^{143}$Nd arrays intersect the ε^{176}Hf axis at values slightly greater (1–2 ε units) than zero (e.g. Blichert-Toft and Albarede, 1997). This may be explained by a small (~1%) hidden reservoir rich in MgPv and/or by the combined Lu–Hf and Sm–Nd CHUR models being not perfectly applicable to BSE.

An important finding of this study is that Lu/Hf fractionations associated with MgPv crystallization from chondritic liquids are muted compared to those produced by MgPv crystallization from peridotitic liquids. Thus, using the partition coefficients derived from the chondrite model predicts less severe decoupling of ε^{176}Hf–ε^{143}Nd, muting the effects of MgPv enrichment or subtraction from observed mantle. However, the ε^{176}Hf $-\varepsilon^{143}$Nd shifts associated with enriching the observed mantle with MgPv are still large enough that only <10% percent subtraction of MgPv from the accessible Earth can be tolerated given the width of the BSE ε^{176}Hf–ε^{143}Nd array where it intersects CHUR. This finding may be used as support for Earth's BSE composition being more chondrite-like and for a small MgPv-enriched hidden reservoir, which would help explain super-chondritic $Ca/Al_{accessible\ Earth}$, but it also serves to highlight the importance of understanding the compositional dependences of trace element partitioning by perovskite.

4.1.3.3. Effects of combined MgPv and CaPv crystallization on Hf–Nd isotopic decoupling In order to explain the current volume of the LLVSPs and the magnitude of Sm/Nd fractionation, the first 90% of crystallization products of the BMO have been proposed to homogenize with the accessible Earth. However, it is likely that CaPv saturates from a BSE liquid composition prior to $F = 0.1$ (e.g. Ito et al., 2004). CaPv has a great affinity for REE + Y + U + Th, and consequently, CaPv fractionation is an efficient mechanism for transferring a wide range of trace elements from the BMO into the overlying mantle. CaPv fractionates many trace elements in the opposite manner as MgPv. For example, CaPv prefers Lu to Hf and REE to HFSE (e.g. Corgne et al., 2005; Hirose et al., 2004; Kato et al., 1996; Taura et al., 2001). Consequently, many of the geochemical signatures associated with MgPv would be muted or even reversed if MgPv fractionation was associated with CaPv fractionation. However, both MgPv and CaPv prefer Sm to Nd, indicating it is possible to generate coupled changes to ε^{142}Nd, ε^{143}Nd, and ε^{176}Hf, provided both CaPv and MgPv are fractionated together and that CaPv dominates Lu/Hf of the sequestered reservoir.

To quantify the effect of CaPv + MgPv coprecipitation in a BMO, we applied the same REE + Y partition coefficient interpolation model used for MgPv to the CaPv partition coefficient data from experiment H2020b of Corgne et al. (2005). This experiment was analyzed by SIMS and LA-ICP-MS, and the resulting data were averaged for the REE + Y interpolation model. Averages of reported partition coefficients for U, Th, Nb, Ta, Zr, Hf, and Ti from experiment H2020b were directly taken to form a complete set of U + Th + REE + Y + HFSE partition coefficients for CaPv.

These partition coefficients for CaPv were used in conjunction with those determined for MgPv to determine a bulk partition coefficient for each element during BMO crystallization. The modal abundance of CaPv in peridotite and chondrite BSE compositions is taken as 7.5%. The resulting bulk partition coefficients are then applied to both batch and near-fractional crystallization calculations ($F = 0.1$). The compositions of MgPv + CaPv produced by the crystallization calculations are then mixed with a reservoir of primitive mantle (representing the mantle overlying the BMO) to calculate the composition of the accessible Earth. Both the application of

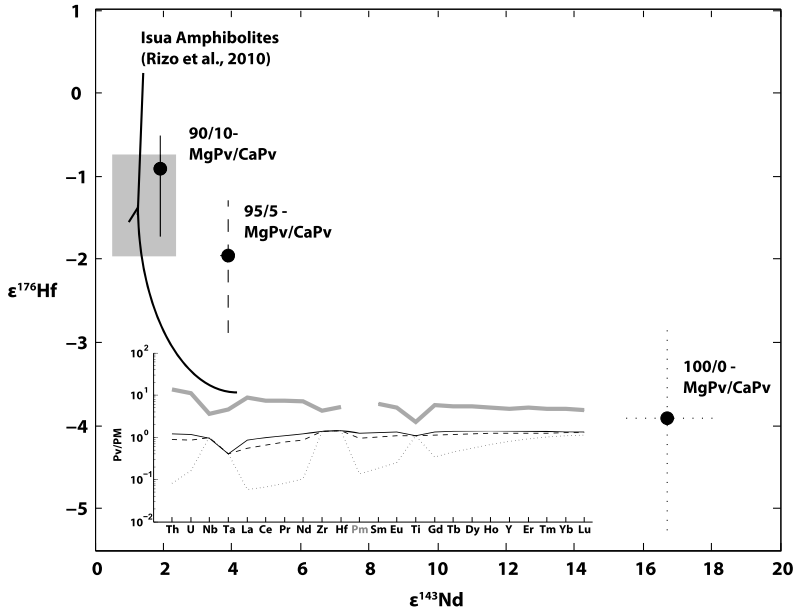

Fig. 8. Plot of ε^{176}Hf–ε^{143}Nd compositions calculated for MgPv ± CaPv cumulates (not mixed with overlying mantle) and field of initial ε^{176}Hf–ε^{143}Nd observed at Isua (grey field redrawn from Rizo et al., 2011). Isotopic evolution of cumulates is calculated starting at 4.5 Ga and ending at 3.7 Ga, and trace element compositions are calculated by integrating the first 70% of cumulates produced by near-fractional crystallization. The line types associated with each symbol (i.e. solid, dashed, and dotted) are mirrored in the inset spidergram plot (black lines). The grey spidergram is the average of amphibolites reported by Rizo et al. (2011). Cumulates with 95:5 and 90:10 for MgPv:CaPv have relatively muted HFSE anomalies and ε^{176}Hf–ε^{143}Nd values similar to the average of amphibolites observed at Isua (grey spidergram and field, Rizo et al., 2011). CHUR evolution parameters are taken from Bouvier et al. (2008). Uncertainties on individual scenarios are those propagated from uncertainties in partition coefficients (one standard deviation).

partition coefficients and mixing calculations follow the approach the approach of the MgPv-only BMO calculations (Section 4.1.3.1). The resulting evolution for ε^{143}Nd and ε^{176}Hf were then calculated (Fig. 7).

Compared to the MgPv-only scenarios, the MgPv + CaPv scenarios result in significantly less ε^{143}Nd and ε^{176}Hf decoupling. This is because CaPv effectively transfers all REEs from the liquid to the solid, forcing REEs in the solid to be in near-chondritic relative proportions. Additionally, the positive HFSE anomalies associated with a MgPv-only BMO are either severely muted or reversed. Thus, a BMO that fluxed MgPv + CaPv into the accessible Earth is a plausible alternative to a BMO that strictly fluxed MgPv.

An interesting implication of a MgPv + CaPv-saturated BMO is that it would be depleted in heat producing elements. The late-stage, dense products of a BMO have been proposed as the source material for large low shear velocity provinces and ultra low velocity zones (LLSVP and ULVZ). If these lower mantle structures are related to the last stages of a BMO that has fractionated significant CaPv, these volumes of mantle could have less thermal buoyancy than the surrounding mantle. Thus, CaPv fractionation from a BMO may help stabilize LLSVPs and ULVZs at the bottom of the mantle over geological time scales.

4.1.3.4. Magma ocean fractionations recorded in Archean crustal rocks? Detailed studies of Archean rocks provide evidence for decoupling of ε^{176}Hf–ε^{143}Nd mantle systematics (Vervoort et al., 1996; Vervoort and Blichert-Toft, 1999, Shirey et al., 2008; Hoffmann et al., 2011; Rizo et al., 2011; Puchtel et al., 2013; Blichert-Toft et al., 1999), in contrast to the modern array of mantle materials. It has long been recognized that MgPv and CaPv are capable of decoupling of ε^{176}Hf–ε^{143}Nd (e.g. Blichert-Toft and Albarede, 1997; Salters and White, 1998). The best documented example of decoupling comes from Isua in west Greenland (~3.8 Ga), where initial ε^{176}Hf–ε^{143}Nd values commonly extend to the right of the modern terrestrial array near the origin (Fig. 8).

This decoupling of ε^{176}Hf–ε^{143}Nd at Isua can be generated by MgPv and CaPv cumulates that co-crystallize from a magma ocean, where the cumulates remain unmixed until ~3.8 Ga (Vervoort et al., 1996; Vervoort and Blichert-Toft, 1999; Caro et al., 2005; Shirey et al., 2008; Hoffmann et al., 2011; Rizo et al., 2011). Our current model supports this hypothesis. Namely, MgPv-rich, CaPv-poor floatation cumulates associated with a BMO would possess positive ε^{143}Nd and nearly chondritic ε^{176}Hf given sufficient time for radiogenic ingrowth, similar to the decoupling observed in at Isua in west Greenland (Fig. 8). As noted by Rizo et al. (2011), pure, or nearly-pure, MgPv cumulates would have strong, positive HFSE anomalies, opposite to the trace element anomalies observed at Isua (e.g. Shirey et al., 2008; Hoffmann et al., 2011; Rizo et al., 2011). These positive HFSE anomalies can be lessened, and even reversed, by including a small CaPv component, while still maintaining the observed ε^{176}Hf–ε^{143}Nd signatures (inset, Fig. 8). Subsequent processing of the Isua mantle source, perhaps related to subduction (e.g. Shirey et al., 2008; Jenner et al., 2009), could impart more pronounced negative HFSE anomalies. Partial melting and low pressure fractionation would act to minimize differences in absolute trace element abundances between average amphibolites (inset of Fig. 8, grey spidergram, Rizo et al., 2011) and the MgPv ± CaPv source (inset of Fig. 8, black spidergrams). Thus, the ε^{176}Hf–ε^{143}Nd and trace element systematics at Isua also support the existence of a BMO that fluxed CaPv and MgPv into the overlying mantle. This scenario would require relatively rapid saturation of CaPv in a BMO in order for CaPv to affect ε^{176}Hf–ε^{143}Nd and trace element systematics observed at Isua at ~3.8 Ga. Alternatively, ε^{176}Hf–ε^{143}Nd and trace element systematics at Isua may also be explained by initially dense MgPv + CaPv cumulates (accumulated at the base of a magma ocean) that were later fluxed into the upper mantle. The mechanism for fluxing into the upper mantle may be entrainment by upwelling material or positive buoyancy of the cumulate itself.

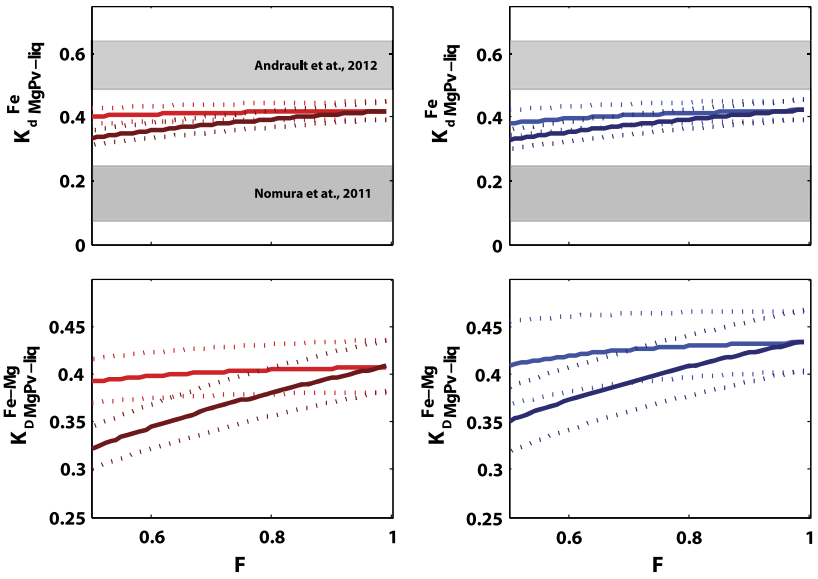

Fig. 9. Calculated $K_{d\,\mathrm{MgPv-liq}}^{\mathrm{Fe}}$ (top row) and $K_{D\,\mathrm{MgPv-liq}}^{\mathrm{Fe-Mg}}$ (bottom row) for different crystallization scenarios (solid lines). Blue curves are for a peridotitic starting composition. Red curves are for a chondritic starting composition. Lighter shades are for batch calculations, and darker shades are for near-fractional calculations. Modeled $K_{d\,\mathrm{MgPv-liq}}^{\mathrm{Fe}}$ values are intermediate to recent experimental determinations (light grey: Andrault et al., 2012, and dark grey: Nomura et al., 2011). The net effect of different bulk compositions on $K_{d\,\mathrm{MgPv-liq}}^{\mathrm{Fe}}$ is small, but compositional effects related to MgPv crystallization cause $K_{d\,\mathrm{MgPv-liq}}^{\mathrm{Fe}}$ to decrease. Dotted lines represent a one standard deviation envelope around the mean value as determined by the Monte Carlo approach. (For interpretation of the references to color in this figure legend, the reader is referred to the web version of this article.)

4.2. Density of silicate liquid and MgPv

The potential dynamics of magma ocean crystallization are controlled, in part, by the relative densities of liquid and solid phases. Fe has a high molar mass compared to Mg, but due to their similar ionic radii and equal charge, Fe^{2+} commonly exchanges for Mg with minimal changes in molar volume (e.g. Mosenfelder et al., 2007). Thus, Fe partitioning between liquid and solid (i.e. $K_{d\,\mathrm{MgPv-liq}}^{\mathrm{Fe}}$) has a strong influence on the density contrast of equilibrium liquid–solid pairs and whether MgPv will float, sink, or remain suspended in a magma ocean. Consequently, the determination of $K_{d\,\mathrm{MgPv-liq}}^{\mathrm{Fe}}$ has been the focus of recent experimental work (Andrault et al., 2012; Nomura et al., 2011). Values of $K_{d\,\mathrm{MgPv-liq}}^{\mathrm{Fe}}$ have been determined in systems with olivine (Si, Fe, Mg-bearing) and chondritic (Si, Al, Fe, Mg, Ca-bearing) starting compositions using LH-DACs. Results from these two studies differ despite ranging over similar pressures and temperatures, suggesting compositional effects on $K_{d\,\mathrm{MgPv-liq}}^{\mathrm{Fe}}$ are substantial (Fig. 9).

Al stabilizes Fe in MgPv via the charge coupled substitution of Fe^{3+} and Al (Andrault et al., 2012; Frost and Langenhorst, 2002; Frost et al., 2004; Mao et al., 1997; McCammon, 1997; Wood, 2000; Wood and Rubie, 1996). We show that the parameterization of $K_{d\,\mathrm{MgPv-liq}}^{\mathrm{Fe}}$ contains a strong positive coefficient for the $X_{\mathrm{sol}}^{\mathrm{Al}}$ term (Table A.1), demonstrating that Al stabilizes Fe in MgPv over the silicate liquid. This indicates that partitioning experiments with lower than naturally applicable Al will systematically underestimate $K_{d\,\mathrm{MgPv-liq}}^{\mathrm{Fe}}$ (cf. Nomura et al., 2011). This analysis does not consider the potential role of spin-transitions (Nomura et al., 2011).

Results from this study predict values of ~0.3–0.4 for $K_{d\,\mathrm{MgPv-liq}}^{\mathrm{Fe}}$ in a peridotitic system (Fig. 9). This range of $K_{d\,\mathrm{MgPv-liq}}^{\mathrm{Fe}}$(~0.3–0.4) is lower than determined for the chondritic LH-DAC experiments (~0.5–0.6) in Andrault et al. (2012). However, given the in-situ analytical technique employed by Andrault et al. (2012), the bulk chemistry of MgPv and equilibrium liquids are unknown except for a single experiment that was quenched and analyzed by an electron microprobe. This analysis indicated that the liquid was enriched in Si (63.2 wt% SiO_2) compared to estimates for the composition of bulk silicate Earth (either peridotitic or chondritic compositions have ~45–50 wt% SiO_2). As noted, the parameterization of $K_{d\,\mathrm{MgPv-liq}}^{\mathrm{Fe}}$ contains a positive $X_{\mathrm{liq}}^{\mathrm{Si}}$ term (Section 2). Consequently, the offset between our model prediction and the experimental determination by Andrault et al. (2012) for $K_{d\,\mathrm{MgPv-liq}}^{\mathrm{Fe}}$ can be explained by chemical differences in the two systems (i.e. the modeled system has lower $X_{\mathrm{liq}}^{\mathrm{Si}}$).

5. Conclusions

A model for MgPv crystallization has been developed and applied to different potential dynamical outcomes for a deep magma ocean. Parameterized REE + Y + U + Th partition coefficients are shown to positively correlate with $X_{\mathrm{sol}}^{\mathrm{Al}}$ and X_{sol}^{Ca} in MgPv. HFSE partition coefficients are shown to positively correlate with $X_{\mathrm{sol}}^{\mathrm{Al}}$ but negatively correlate with X_{sol}^{Ca} in MgPv. These correlations accord with trace element substitutional mechanisms observed in pyroxenes. $K_{d\,\mathrm{MgPv-liq}}^{\mathrm{Fe}}$ is a strong, positive function of $X_{\mathrm{sol}}^{\mathrm{Al}}$ and is moderately incompatible ($K_{d\,\mathrm{MgPv-liq}}^{\mathrm{Fe}} = 0.3$–$0.4$). The partition coefficient parameterizations have been applied to a series crystallization models in order to quantify the geochemical consequences associated with MgPv enrichment and depletion in the accessible Earth. The predicted geochemical consequences of MgPv enrichment or depletion are not observed. Thus, the current analysis suggests that (1) earliest crystallizing solids (MgPv) in a magma ocean remained entrained and did not fractionate from the liquid (2) fractionations were small so that their net effect on the accessible Earth is obscured, (3) or large-scale fractionations of MgPv have largely been homogenized, leaving little net geochemical effect on BSE. A BMO that fluxes CaPv + MgPv into the accessible Earth mutes many of the unobserved geochemical effects associated with a MgPv-only BMO and can explain the ε^{176}Hf–ε^{143}Nd systematics observed at Isua, and consequently offers an alternative possibility for BMO evolution that is depleted in heat producing elements.

Acknowledgements

We thank the three anonymous reviewers for their comments and suggestions. We additionally thank Don Forsyth for his assistance developing the crystallization model. Discussions with Abby Kavner and Quentin Williams substantially improved the manuscript. Leah B. Ziegler acknowledges support from NSF-1049579. Dave R. Stegman acknowledges support from NSF-1255040. Matt G. Jackson acknowledges support from NSF-1153894. All authors acknowledge support from 2012 Cooperative Institute for Dynamic Earth Research (CIDER-II) workshop supported by NSF-1135452.

Appendix A. Supplementary material

Supplementary material related to this article can be found online at http://dx.doi.org/10.1016/j.epsl.2014.01.028.

References

Agee, C.B., 1990. A new look at differentiation of the Earth from melting experiments on the Allende meteorite. Nature 346, 834–837.

Andrault, D., Bolfan-Casanova, N., Lo Nigro, G., Bouhifd, M.A., Garbarino, G., Mezouar, M., 2011. Solidus and liquidus profiles of chondritic mantle: Implication for melting of the Earth across its history. Earth Planet. Sci. Lett. 304, 251–259.

Andrault, D., Petitgirard, S., Lo Nigro, G., Devidal, J.-L., Veronesi, G., Garbarino, G., Mezouar, M., 2012. Solid–liquid iron partitioning in Earth's deep mantle. Nature 487, 354–357.

Asahara, Y., Kubo, T., Kondo, T., 2004. Phase relations of a carbonaceous chondrite at lower mantle conditions. Phys. Earth Planet. Inter. 143, 421–432.

Blichert-Toft, J., Albarede, F., 1997. The Lu–Hf isotope geochemistry of chondrites and the evolution of the mantle–crust system. Earth Planet. Sci. Lett. 148, 243–258.

Blichert-Toft, J., Albarède, F., Rosing, M., Frei, R., Bridgwater, D., 1999. The Nd and Hf isotopic evolution of the mantle through the Archean. Results from the Isua supracrustals, West Greenland, and from the Birimian terranes of West Africa. Geochim. Cosmochim. Acta 63, 3901–3914.

Bouvier, A., Vervoort, J.D., Patchett, P.J., 2008. The Lu–Hf and Sm–Nd isotopic composition of CHUR: Constraints from unequilibrated chondrites and implications for the bulk composition of terrestrial planets. Earth Planet. Sci. Lett. 273, 48–57.

Boyet, M., Carlson, R.W., 2005. ^{142}Nd evidence for early (>4.53 Ga) global differentiation of the silicate earth. Science 309, 576–581.

Burke, K., Steinberger, B., Torsvik, T.H., Smethurst, M.A., 2008. Plume generation zones at the margins of large low shear velocity provinces on the core–mantle boundary. Earth Planet. Sci. Lett. 265, 49–60.

Canup, R., 2004. Simulations of a late lunar-forming impact. Icarus 168, 433–456.

Caro, G., Bourdon, B., 2010. Non-chondritic Sm/Nd ratio in the terrestrial planets: Consequences for the geochemical evolution of the mantle crust system. Geochim. Cosmochim. Acta 74, 3333–3349.

Caro, G., Bourdon, B., Wood, B.J., Corgne, A., 2005. Trace-element fractionation in Hadean mantle generated by melt segregation from a magma ocean. Nature 436, 246–249.

Chambers, J.E., Wetherill, G.W., 1998. Making the terrestrial planets: N-body integrations of planetary embryos in three dimensions. Icarus 136, 304–327.

Chauvel, C., Lewin, E., Carpentier, M., Arndt, N.T., Marini, J.-C., 2008. Role of recycled oceanic basalt and sediment in generating the Hf–Nd mantle array. Nat. Geosci. 1, 64–67.

Coltice, N., Moreira, M., Hernlund, J., Labrosse, S., 2011. Crystallization of a basal magma ocean recorded by helium and neon. Earth Planet. Sci. Lett. 308, 193–199.

Corgne, A., Liebske, C., Wood, B.J., Rubie, D.C., Frost, D.J., 2005. Silicate perovskite-melt partitioning of trace elements and geochemical signature of a deep perovskitic reservoir. Geochim. Cosmochim. Acta 69, 485–496.

de Koker, N., Karki, B.B., Stixrude, L., 2013. Thermodynamics of the MgO–SiO_2 liquid system in Earth's lowermost mantle from first principles. Earth Planet. Sci. Lett. 361, 58–63.

Drake, M.J., McFarlane, E.A., Gasparik, T., Rubie, D.C., 1993. Mg-perovskite/silicate melt and majorite garnet/silicate melt partition coefficients in the system CaO–MgO–SiO_2 at high temperatures and pressures. J. Geophys. Res., Planets 98, 5427–5431.

Fiquet, G., Auzende, A.L., Siebert, J., Corgne, A., Bureau, H., Ozawa, H., Garbarino, G., 2010. Melting of peridotite to 140 gigapascals. Science 329, 1516–1518.

Frost, D.J., Langenhorst, F., 2002. The effect of Al_2O_3 on Fe–Mg partitioning between magnesiowustite and magnesium silicate perovskite. Earth Planet. Sci. Lett. 199, 227–241.

Frost, D.J., Liebske, C., Langenhorst, F., McCammon, C.A., Tronnes, R.G., Rubie, D.C., 2004. Experimental evidence for the existence of iron-rich metal in the Earth's lower mantle. Nature 428, 409–412.

Garnero, E.J., McNamara, A.K., 2008. Structure and dynamics of Earth's lower mantle. Science 320, 626–628.

Hirose, K., Shimizu, N., van Westrenen, W., Fei, Y.W., 2004. Trace element partitioning in Earth's lower mantle and implications for geochemical consequences of partial melting at the core–mantle boundary. Phys. Earth Planet. Inter. 146, 249–260.

Hoffmann, J., Münker, C., Polat, A., Rosing, M.T., Schulz, T., 2011. The origin of decoupled Hf–Nd isotope compositions in Eoarchean rocks from southern West Greenland. Geochim. Cosmochim. Acta 75, 6610–6628.

Huang, S., Jacobsen, S.B., Mukhopadhyay, S., 2013. ^{147}Sm–^{143}Nd systematics of Earth are inconsistent with a superchondritic Sm/Nd ratio. Proc. Natl. Acad. Sci. USA 110, 4929–4934.

Ito, E., Takahashi, E., 1987. Melting of peridotite at uppermost lower mantle conditions. Nature 328, 514–517.

Ito, E., Kubo, A., Katsura, T., Walter, M.J., 2004. Melting experiments of mantle materials under lower mantle conditions with implications for magma ocean differentiation. Phys. Earth Planet. Inter. 143, 397–406.

Jenner, F.E., Bennett, V.C., Nutman, A.P., Friend, C.R.L., Norman, M.D., Yaxley, G., 2009. Evidence for subduction at 3.8 Ga: Geochemistry of arc-like metabasalts from the southern edge of the Isua Supracrustal Belt. Chem. Geol. 261, 83–98.

Kato, T., Ringwood, A.E., Irifune, T., 1988a. Constraints on element partition coefficients between $MgSiO_3$ perovskite and liquid determined by direct measurements. Earth Planet. Sci. Lett. 90, 65–68.

Kato, T., Ringwood, A.E., Irifune, T., 1988b. Experimental determination of element partitioning between silicate perovskites, garnets, and liquids: constraints on Earth differentiation of the mantle. Earth Planet. Sci. Lett. 89, 123–145.

Kato, T., Ohtani, E., Ito, Y., Onuma, K., 1996. Element partitioning between silicate perovskites and calcic ultrabasic melt. Phys. Earth Planet. Inter. 96, 201–207.

Labrosse, S., Hernlund, J.W., Coltice, N., 2007. A crystallizing dense magma ocean at the base of the Earth's mantle. Nature 450, 866–869.

Li, J., Agee, C.B., 1996. Geochemistry of mantle–core differentiation at high pressure. Nature 381, 686–689.

Liebske, C., Frost, D.J., 2012. Melting phase relations in the MgO–$MgSiO_3$ system between 16 and 26 GPa: Implications for melting in Earth's deep interior. Earth Planet. Sci. Lett. 345, 159–170.

Liebske, C., Corgne, A., Frost, D.J., Rubie, D.C., Wood, B.J., 2005. Compositional effects on element partitioning between Mg-silicate perovskite and silicate melts. Contrib. Mineral. Petrol. 149, 113–128.

Lodders, K., 2003. Solar system abundances and condensation temperatures of the elements. Astrophys. J. 591, 1220–1247.

Mao, H.K., Shen, G.Y., Hemley, R.J., 1997. Multivariable dependence of Fe–Mg partitioning in the lower mantle. Science 278, 2098–2100.

McCammon, C., 1997. Perovskite as a possible sink for ferric iron in the lower mantle. Nature 387, 694–696.

McDonough, W.F., Sun, S.S., 1995. The composition of the Earth. Chem. Geol. 120, 223–253.

McFarlane, E.A., Drake, M.J., Rubie, D.C., 1994. Element partitioning between Mg-perovskite, magnesiowustite, and silicate melt at conditions of the Earth's mantle. Geochim. Cosmochim. Acta 58, 5161–5172.

Mosenfelder, J.L., Asimow, P.D., Ahrens, T.J., 2007. Thermodynamic properties of Mg_2SiO_4 liquid at ultra-high pressures from shock measurements to 200 GPa on forsterite and wadsleyite. J. Geophys. Res., Solid Earth 112.

Mosenfelder, J.L., Asimow, P.D., Frost, D.J., Rubie, D.C., Ahrens, T.J., 2009. The $MgSiO_3$ system at high pressure: Thermodynamic properties of perovskite, postperovskite, and melt from global inversion of shock and static compression data. J. Geophys. Res., Solid Earth 114.

Nomura, R., Ozawa, H., Tateno, S., Hirose, K., Hernlund, J., Muto, S., Ishii, H., Hiraoka, N., 2011. Spin crossover and iron-rich silicate melt in the Earth's deep mantle. Nature 473, 199–202.

Ohtani, E., Moriwaki, K., Kato, T., Onuma, K., 1998. Melting and crystal–liquid partitioning in the system Mg_2SiO_4–Fe_2SiO_4 to 25 GPa. Phys. Earth Planet. Inter. 107, 75–82.

O'Neill, H.S.C., Palme, H., 2008. Collisional erosion and the non-chondritic composition of the terrestrial planets. Philos. Trans. R. Soc., Math. Phys. Eng. Sci. 366, 4205–4238.

O'Nions, R.K., Oxburgh, E.R., 1983. Heat and helium in the Earth. Nature 306, 429–431.

Presnall, D.C., Weng, Y.H., Milholland, C.S., Walter, M.J., 1998. Liquidus phase relations in the system MgO–$MgSiO_3$ at pressures up to 25 GPa—constraints on crystallization of a molten Hadean mantle. Phys. Earth Planet. Inter. 107, 83–95.

Puchtel, I., Blichert-Toft, J., Touboul, M., Walker, R., Byerly, G., Nisbet, E., Anhaeusser, C., 2013. Insights into early Earth from Barberton komatiites: Evidence from lithophile isotope and trace element systematics. Geochim. Cosmochim. Acta 108, 63–90.

Ranen, M.C., Jacobsen, S.B., 2006. Barium isotopes in chondritic meteorites: Implications for planetary reservoir models. Science 314, 809–812.

Righter, K., Drake, M.J., Yaxley, G., 1997. Prediction of siderophile element metal–silicate partition coefficients to 20 GPa and 2800 °C: The effects of pressure, temperature, oxygen fugacity, and silicate and metallic melt compositions. Phys. Earth Planet. Inter. 100, 115–134.

Rizo, H., Boyet, M., Blichert-Toft, J., Rosing, M., 2011. Combined Nd and Hf isotope evidence for deep-seated source of Isua lavas. Earth Planet. Sci. Lett. 312, 267–279.

Rubie, D.C., Frost, D.J., Mann, U., Asahara, Y., Nimmo, F., Tsuno, K., Kegler, P., Holzheid, A., Palme, H., 2011. Heterogeneous accretion, composition and core–mantle differentiation of the Earth. Earth Planet. Sci. Lett. 301, 31–42.

Salters, V.J.M., White, W.M., 1998. Hf isotope constraints on mantle evolution. Chem. Geol. 145, 447–460.

Sanloup, C., Drewitt, J.W., Konôpková, Z., Dalladay-Simpson, P., Morton, D.M., Rai, N., van Westrenen, W., Morgenroth, W., 2013. Structural change in molten basalt at deep mantle conditions. Nature 503, 104–107.

Shirey, S.B., Kamber, B.S., Whitehouse, M.J., Mueller, P.A., Basu, A.R., 2008. A review of the isotopic and trace element evidence for mantle and crustal processes in the Hadean and Archean: Implications for the onset of plate tectonic subduction. When Did Plate Tectonics Begin on Planet Earth?. Spec. Pap., Geol. Soc. Am. 440, 1.

Solomatov, V., 2000. Fluid dynamics of a terrestrial magma ocean. In: Origin of the Earth and Moon, vol. 1, pp. 323–338.

Solomatov, V.S., Stevenson, D.J., 1993. Suspension in convective layers and style of differentiation of a terrestrial magma ocean. J. Geophys. Res., Planets 98, 5375–5390.

Stixrude, L., Karki, B., 2005. Structure and freezing of $MgSiO_3$ liquid in Earth's lower mantle. Science 310, 297–299.

Stixrude, L., de Koker, N., Sun, N., Mookherjee, M., Karki, B.B., 2009. Thermodynamics of silicate liquids in the deep Earth. Earth Planet. Sci. Lett. 278, 226–232.

Taura, H., Yurimoto, H., Kato, T., Sueno, S., 2001. Trace element partitioning between silicate perovskites and ultracalcic melt. Phys. Earth Planet. Inter. 124, 25–32.

Thomas, C.W., Liu, Q., Agee, C.B., Asimow, P.D., Lange, R.A., 2012. Multi-technique equation of state for Fe_2SiO_4 melt and the density of Fe-bearing silicate melts from 0 to 161 GPa. J. Geophys. Res., Solid Earth 117.

Tonks, W., Melosh, H., 1990. The physics of crystal settling and suspension in a turbulent magma ocean. In: Origin of the Earth, vol. 1, pp. 151–174.

Tronnes, R.G., 2000. Melting relations and major element partitioning in an oxidized bulk Earth model composition at 15–26 GPa. Lithos 53, 233–245.

Tronnes, R.G., Frost, D.J., 2002. Peridotite melting and mineral–melt partitioning of major and minor elements at 22–24.5 GPa. Earth Planet. Sci. Lett. 197, 117–131.

Vervoort, J.D., Blichert-Toft, J., 1999. Evolution of the depleted mantle: Hf isotope evidence from juvenile rocks through time. Geochim. Cosmochim. Acta 63, 533–556.

Vervoort, J.D., Patchett, P.J., Gehrels, G.E., Nutman, A.P., 1996. Constraints on early Earth differentiation from hafnium and neodymium isotopes. Nature 379, 624–627.

Walter, M.J., Nakamura, E., Tronnes, R.G., Frost, D.J., 2004. Experimental constraints on crystallization differentiation in a deep magma ocean. Geochim. Cosmochim. Acta 68, 4267–4284.

Wetherill, G.W., 1985. Occurrence of giant impacts during the growth of the terrestrial planets. Science 228, 877–879.

Wood, B.J., 2000. Phase transformations and partitioning relations in peridotite under lower mantle conditions. Earth Planet. Sci. Lett. 174, 341–354.

Wood, J.A., Dickey Jr., J., Marvin, U.B., Powell, B., 1970. Lunar anorthosites and a geophysical model of the moon. Geochim. Cosmochim. Acta, Suppl. 1, 965.

Wood, B.J., Rubie, D.C., 1996. The effect of alumina on phase transformations at the 660-kilometer discontinuity from Fe–Mg partitioning experiments. Science 273, 1522–1524.

Yao, L., Sun, C., Liang, Y., 2012. A parameterized model for REE distribution between low-Ca pyroxene and basaltic melts with applications to REE partitioning in low-Ca pyroxene along a mantle adiabat and during pyroxenite-derived melt and peridotite interaction. Contrib. Mineral. Petrol. 164, 261–280.

Zhang, J.Z., Herzberg, C., 1994. Melting experiments on anhydrous peridotite KLB-1 from 5.0 to 22.5 GPa. J. Geophys. Res., Solid Earth 99, 17729–17742.

Ziegler, L.B., Stegman, D.R., 2013. Implications of a long-lived basal magma ocean in generating Earth's ancient magnetic field. Geochem. Geophys. Geosyst. 14, 4735–4742.